Improved first-principles equation-of-state table of deuterium for high-energy-density applications

D. I. Mihaylov,* V. V. Karasiev, S. X. Hu, J. R. Rygg, V. N. Goncharov, and G. W. Collins
Laboratory for Laser Energetics, University of Rochester, 250 East River Road, Rochester, New York 14623-1299, USA

(Received 28 May 2021; revised 20 August 2021; accepted 23 September 2021; published xxxxxxxxxx)

We present a first-principles equation-of-state (EOS) table of deuterium aimed at improving the previously established first-principles equation-of-state table (FPEOS) [S. X. Hu *et al.*, Phys. Rev. B **84**, 224109 (2011); S. X. Hu *et al.*, Phys. Plasmas **22**, 056304 (2015)]. The EOS table presented here, referred to as iFPEOS, introduces (1) a universal density functional theory (DFT) treatment of all density and temperature conditions, (2) a fully consistent treatment of exchange-correlation (XC) thermal effects across the entire range of temperatures covered, and (3) quantum treatment of ions. Based on *ab initio* molecular dynamics driven by *thermal* density functional theory, iFPEOS includes density points in the range $1\times10^{-3} \leqslant \rho \leqslant 1.6\times10^{3}$ g/cm^3 and temperature points in the range 800 K $\leqslant T \leqslant$ 256 MK, thus covering the challenging warm dense matter (WDM) regime. For an improved description of the electronic structure, iFPEOS employs an advanced free-energy XC density functional with explicit temperature dependence, which is at the metageneralized gradient approximation level of DFT. We use the latest orbital-free free-energy density functional for the high-temperature regime where it shows excellent agreement with standard Mermin-Kohn-Sham DFT. For quantum treatment of ions we use path-integral molecular dynamics in order to take into account nuclear quantum effects. Results are compared to other EOS models and most recent experimental measurements of deuterium properties such as the molecular-to-atomic fluid transition, the principal and reshock Hugoniot, and sound speed. We find that iFPEOS provides an improved agreement with experimental data compared to other first-principles EOS models in the WDM regime for pressures up to 200 GPa and temperatures up to 60 000 K. For higher pressures and temperatures, however, iFPEOS is in agreement with other models in predicting lower compressibility and higher sound speed along the Hugoniot, compared to experiment.

DOI: 10.1103/PhysRevB.00.004100

I. INTRODUCTION AND MOTIVATION

Accurate knowledge of the deuterium (D) EOS table is of particular interest to a broad and interdisciplinary group of researchers. A reliable EOS model of D covering a wide range of densities and temperatures is required in the design of inertial confinement fusion (ICF) targets, where EOS information is critical in determining important parameters such as the compressibility of the deuterium-tritium fuel [1], shock wave timing [2], and Rayleigh-Taylor instability growth rates [3]. In addition, an accurate EOS table of hydrogen, which can be directly obtained by that of D through mass scaling, is also important to the fields of planetary and stellar physics [4]. Yet, even though D is an isotope of the simplest element in the periodic table, its properties under extreme conditions have long been a subject of extensive research and still present challenges [5–7].

Recently, a comprehensive review and analysis of available models for the EOS of deuterium was published by Gaffney *et al.* [8], where EOS models based on drastically different methodologies such as the chemical model [9,10], *ab initio* molecular dynamics (AIMD) in combination with path-integral Monte Carlo (PIMC) [11–13], AIMD driven by orbital-free (OF) DFT (OFMD) [14–16], etc., were discussed. The main conclusions reached in [8] highlight the lack of systematic agreement between the different D EOS models across a wide range of thermodynamic conditions and the inability of any one single model to match experimental measurements at all ρ-T regimes. The same is true for other widely used EOS models such as the SCvH (Saumon, Chabrier, van Horn) [17] and its subsequent improvement in the high-density, high-temperature regime by Chabrier *et al.* [18]. Following the review by Gaffney *et al.*, new experimental measurements of shocked D by Fernandez-Pañella *et al.* [5] at a previously unexplored pressure regime ($250 < P < 550$ GPa) further confirm the lack of a single, standout model for the EOS table of D. As shown in Fig. 2 of Ref. [5], models which agree with experimental measurements of the principal and reshock Hugoniot at low P fail to do so in the high-P regime and vice versa. Furthermore, secondary shock measurements which are also reported in Ref. [5] are underestimated by first-principles EOS models by 5%–10% for pressures above 600 GPa. In comparison with other recently reported experimental work by Fratanduono *et al.* [6] on the sound speed in shock-compressed D along the principal Hugoniot, recent models are in relatively good agreement with experiment in the low-P regime below 75 GPa, but the disagreement systematically grows as T and P are increased.

Despite all the uncertainty among the different models, one clear trend emerges, namely, that the DFT-based predictions of the principal Hugoniot, such as first-principles

*dmih@lle.rochester.edu

equation-of-state (FPEOS) [11,19,20], Caillabet *et al.* [21] and Karasiev *et al.* [22] are all in good agreement with latest experimental data for the low-P, low-T part of the principal Hugoniot, however, in the high-P, high-T regime there is a systematic underestimation of the compressibility. One of the drawbacks of FPEOS is that it is based on two different methodologies: AIMD with PBE XC for the low-T part and PIMC for the high-T part. This introduces a thermodynamic inconsistency across the two T regimes as thermal effects are fully taken into account by the PIMC method but insufficiently accounted for by the zero-temperature PBE XC. Therefore, one of the main motivations for updating FPEOS is to maintain thermodynamic consistency by fully accounting for T effects across the entire table.

Additionally, iFPEOS was further motivated by the need to investigate the potential improvement in accuracy by an exchange-correlation (XC) density functional at a level beyond the generalized gradient approximation (GGA). Two of the latest DFT-based Hugoniot calculations are those by Caillabet *et al.* [21], where the zero-temperature PBE XC functional is used, and those by Karasiev, which are based on the thermal KDT16 functional [23]. PBE and KDT16 are both at the GGA level of DFT and their only difference is that KDT16, as a finite-T extension of PBE, is designed to take into account XC thermal effects (see Sec. II A for a detailed discussion of finite-T XC functionals). While both predictions appear at significantly lower compressibility compared to latest measurements, KDT16 is ~2.5% closer than PBE. This improvement in accuracy is likely due to XC thermal effects which are taken into account by KDT16. KDT16 is limited, however, in its accuracy by the GGA level of refinement which poses the important question of how a more-advanced thermal XC functional would perform.

Recently, Hinz *et al.* [24] performed an accurate calculation of the insulator-to-metal transition (IMT) boundary in warm dense H and D and showed that this transition is caused by molecular dissociation of H_2/D_2 to atomic H/D (see Fig. 1). The method employed in Ref. [24] used conceptually and procedurally consistent DFT calculations based on path-integral molecular dynamics (PIMD) [25] for including nuclear quantum effects (NQEs), and SCAN-L+rVV10 [26,27] XC functional for treatment of electrons. A combination of the original, orbital-dependent SCAN functional [28] with the rVV10 correction has been recently shown to provide an accurate description of the interaction energies for the molecular dimers due to the accurate treatment of van der Waals interactions [29], which further explains the ability of the SCAN-L+rVV10 method in predicting the IMT boundary. The improvement in accuracy of van der Waals functionals is further demonstrated in [30]. Therefore, the success of this method in solving this long-standing problem, where other XC functionals such as PBE have failed [31], serves as our main motivation for applying a similar but, as will be explained later, improved methodology to obtain iFPEOS. Additionally, iFPEOS was further motivated by recent developments of advanced free-energy density functionals which provide improved accuracy across temperature regimes (see Sec. II for details).

Figure 1 shows the D_2 dissociation boundary as predicted by iFPEOS compared to that by Hinz *et al.* and also to a PBE-based prediction and latest experimental measurements. Here, we do not calculate the dc conductivity in order to determine the IMT boundary, but as is shown in Ref. [24], the IMT boundary is directly related to molecular dissociation. The iFPEOS-predicted molecular dissociation boundary plotted in Fig. 1 has been determined by the pressure drop which occurs as molecular D_2 dissociates into atomic D with rising T along the four, most-relevant isochores (green circles in Fig. 1). Extra calculations at 500, 600, and 700 K were performed in order to determine the lowest-T point. Although iFPEOS does not sample the P-T region as finely, results are in good agreement with those presented in Ref. [24], and the improvement to the PBE-based prediction (green line in Fig. 1) is evident. Furthermore, as suggested by the results in [24], NQEs, taken into account by PIMD, become more and more important at higher pressures and at $P \sim 250$ GPa NQEs appear to significantly lower the IMT boundary. Other studies that show the importance of NQEs at a variety of thermodynamic conditions, especially for light elements such as H and its isotopes [31–34], also serve as motivation to employ PIMD in iFPEOS since in FPEOS ions are treated classically. In summary, the work presented here was motivated by (1) the excellent ability of the SCAN-L+rVV10 method to describe the H/D IMT boundary; (2) recent theoretical developments in finite-T DFT including advanced thermal SCAN-L meta-GGA XC functional; and (3) the need to take into account NQEs.

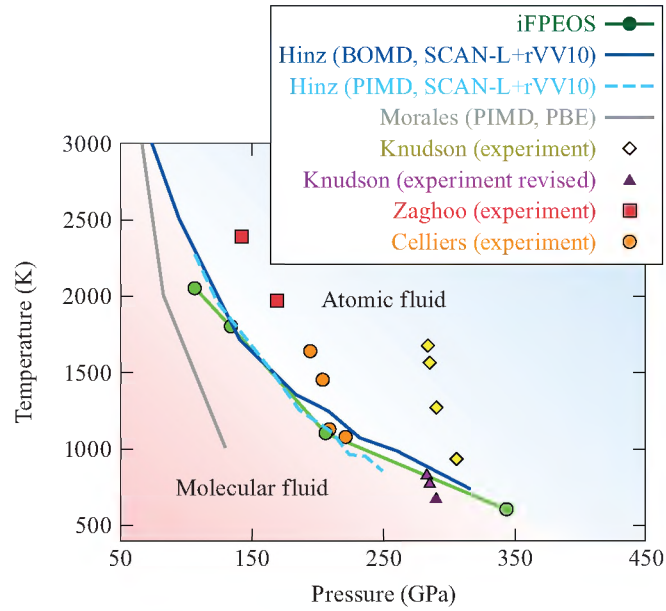

FIG. 1. The dissociation boundary from molecular D_2 to atomic D according to latest experimental measurements [7,32,35], iFPEOS (green curve), SCAN-L+rVV10 [24] (light blue dashed curve: PIMD, solid blue curve: BOMD) and PIMD with PBE XC [31] (gray solid curve). The molecular dissociation boundary according to iFPEOS has been determined along four isochores: 1.45, 1.59, 1.96, and 2.45 g/cm^3 and the P-T conditions at which dissociation occurs are shown with green circles with the lowest-ρ isochore dissociation point appearing at 107 GPa and highest at 344 GPa.

The remainder of this paper is organized as follows: The methods used in this work are described in Sec. II where we

provide detailed outlines of the T-dependent T-SCAN-L XC functional (Sec. II A) and the LKTFγTF orbital-free noninteracting free-energy functional (Sec. II B) and a brief summary of the PIMD method in Sec. II C. Section III provides computational details about all Kohn-Sham molecular dynamics (KSMD) and OFMD simulations, outlines the procedure of tuning LKTFγTF, and presents evidence of the excellent agreement between KSMD and OFMD with tuned LKTFγTF at high T across the entire density range. Section IV provides details about PIMD simulations and presents results about the importance of NQEs across ρ and T regimes covered in iFPEOS. In Sec. V we compare iFPEOS and other select EOS models with some of the latest experimental measurements of warm, dense D such as Hugoniot and sound speed measurements. Finally, Sec. VI summarizes the work presented here. The full iFPEOS table is provided in the Supplemental Material (SM) [36].

II. METHODS

AIMD, where ionic motion is treated classically based on forces calculated by Mermin-Kohn-Sham (MKS) DFT with a ground-state XC functional, has been a very successful method for simulating matter at a wide range of thermodynamic conditions [37–42]. We apply the same methodology to iFPEOS, but also introduce two major improvements: (1) we improve on the DFT ground-state approximation (GSA) by using a recently developed meta-GGA XC free-energy density functional T-SCAN-L [43] to take into account XC thermal effects; and (2) we go beyond the classical treatment of ions by taking into account NQEs via PIMD. Additionally, in the high-T regime, where the MKS treatment is too computationally expensive, we use OF DFT with the recently developed noninteracting free-energy functional LKTFγTF [44].

A. T-SCAN-L free-energy XC density functional

Mermin's extension of the Hohenberg-Kohn theorems to finite T leads to the MKS formalism, which extends the ground-state DFT approach to systems at finite T in thermodynamic equilibrium [38,45]. The MKS formalism formally defines a free-energy density functional; however, currently, the most popular exchange-correlation approximations used in finite-T DFT simulations are ground-state density functionals, which only implicitly depend on T through the T-dependent density [46,47]. Demonstrations of GSA deficiencies to accurately predict physical properties for specific systems at certain thermodynamic conditions were presented in studies of Ref. [48]. Recently, there has been major progress in developing *thermal* functionals, which are true XC free-energy density functionals with explicit T dependence [23,49,50]. In Ref. [49], Karasiev *et al.* introduce the KSDT (Karasiev-Sjostrom-Dufty-Trickey, also see corrKSDT in SM of Ref. [23]) thermal XC functional at the local density approximation (LDA) level of DFT. In Ref. [23], Karasiev *et al.* introduce the GGA-level thermal functional KDT16 (Karasiev-Dufty-Trickey 2016) which, by construction, reduces to the PBE exchange-correlation at the zero-T limit. The improvement in accuracy at elevated T provided by (corr)KSDT and KDT16 has been presented in [22,48,51]. In particular, in Ref. [22], KDT16 is shown to predict a significantly softer, and in better agreement with experimental measurement, principal Hugoniot of D in the high-T/high-P range, where XC thermal effects are important. It is clear that KDT16 captures XC thermal effects at the GGA level of theory, however, due to the fact that KDT16 reduces to PBE as T approaches zero, its accuracy is inherently limited to that of PBE at low T. As a next step to create a thermal XC functional at a higher level of accuracy, Karasiev *et al.* presented a thermal XC functional at the meta-GGA level: the T-SCAN-L functional [43]. This is accomplished by adding the dominating GGA-level XC thermal correction provided by KDT16 to the ground-state SCAN-L meta-GGA XC functional [26] (the deorbitalized version of the advanced SCAN [28] functional):

$$\mathcal{F}_{\rm xc}^{\text{T-SCAN-L}}[n,T] = E_{\rm xc}^{\text{SCAN-L}}[n] + \Delta\mathcal{F}_{\rm xc}^{\rm GGA}[n,T],$$
$$\Delta\mathcal{F}_{\rm xc}^{\rm GGA}[n,T] = \mathcal{F}_{\rm xc}^{\rm KDT16}[n,T] - E_{\rm xc}^{\rm PBE}[n], \quad (1)$$

where $\Delta\mathcal{F}_{\rm xc}^{\rm GGA}[n,T]$ is an additive thermal correction that reduces to zero in the limit $T \to 0$ K. Therefore, at low T, T-SCAN-L reduces to the ground-state SCAN-L functional and at elevated temperatures XC thermal effects are provided by the GGA-level thermal correction. Consequently, T-SCAN-L is an improvement to both SCAN-L and KDT16 because it retains the meta-GGA-level accuracy of SCAN-L at low T and accounts for the dominating XC thermal effects through the KDT16 additive thermal correction. In Ref. [43], T-SCAN-L is shown to provide significant improvement to both SCAN-L and KDT16 in DFT simulations of warm dense matter. In addition, T-SCAN-L is shown to be in good agreement with reference PIMC data [52] in EOS calculations of helium in the T range 125 kK $< T <$ 250 kK. Finally, we combine T-SCAN-L with the rVV10 [27] functional to take into account long-range van der Waals interactions, resulting currently in the most-advanced treatment of XC effects applied to obtain an EOS model.

B. LKTFγTF orbital-free noninteracting free-energy density functional

It is well known that at high-T conventional Kohn-Sham (KS) DFT becomes prohibitively expensive due to the growing number of thermally occupied KS orbitals that need to be included in the calculation. OF DFT mitigates this problem by replacing the exact, orbital-dependent noninteracting kinetic energy with a density functional, e.g., the local Thomas-Fermi (TF) kinetic energy [53,54] or within semilocal approximations [55,56]. Generalization of OF DFT to finite T has led to the development of several noninteracting free-energy density functionals [14,15,57–60]. In this work we employ one of the latest developments in OF noninteracting free-energy density functionals. In particular, we use the LKTF GGA functional [60] in combination with thermal TF [57]. A convex combination of the LKTF functional and TF results in the one-parameter tunable OF GGA functional that preserves the correct high-T limit:

$$\mathcal{F}_s^{\text{LKTF}\gamma\text{TF}}[n,T] = \gamma\mathcal{F}_s^{\text{LKTF}}[n,T] + (1-\gamma)\mathcal{F}_s^{\text{TF}}[n,T], \quad (2)$$

where γ is a free parameter that varies from 0 to 1 [44]. The value of γ is determined such that OF calculations at certain

thermodynamic conditions return results for desired variables that match results from a reference KS calculation. The γ-tuned LKTFγTF is then transferable to other thermodynamic conditions within a transferability domain. In their original work introducing the LKTF functional [60], Luo *et al.* show that at low T, LKTF underestimates P and TF overestimates it compared to a reference KS calculation, and as T increases, agreement with KS calculation improves for both functionals (see Fig. 7 in Ref. [60] for D at $\rho = 1.963\,61$ g/cm^3, $2.7 < T < 8.2$ eV). LKTFγTF, with appropriately tuned γ, agrees, by definition, with the reference KS calculation at the thermodynamic conditions at which the tuning is performed and, as Karasiev *et al.* show [44], the γ-tunable functional shows excellent transferability to higher T along the same isochore. Here we tune γ to match results from reference KS calculations for pressure at the highest iFPEOS T points achievable with KSMD on select ρ points and use this γ for the higher-T points along the same isochore (see Sec. III for details and comparison between OFMD with LKTFγTF and KSMD at select ρ-T conditions).

C. Path-integral molecular dynamics

The ring-polymer PIMD method, where the quantum ion is modeled by a fictitious system of $\mathcal{P}$ number of beads connected circularly via harmonic springs forming a closed flexible polymer, has emerged as a powerful tool for going beyond the Born-Oppenheimer approximation and taking into account NQEs [25,61–67]. Here we provide the relevant equations for energy and pressure derived from the path-integral representation of the partition function with a Hamiltonian for free and interacting ions and electrons (for a detailed derivation, see Refs. [25,34]). For a system of N identical interacting ring polymers with mass M at temperature T, the kinetic and potential energies are expressed as

$$E_{\text{kin}} = \frac{3}{2}N\mathcal{P}k_BT - \sum_{s=1}^{\mathcal{P}}\sum_{i=1}^{N}\frac{1}{2}M\omega_{\mathcal{P}}^2\left(\mathbf{R}_i^{(s)} - \mathbf{R}_i^{(s+1)}\right)^2, \quad (3)$$

$$E_{\text{pot}} = \frac{1}{\mathcal{P}}\sum_{s=1}^{\mathcal{P}} E[\{\phi_j\}^{(s)}, \{\mathbf{R}_i\}^{(s)}], \quad (4)$$

where k_B is the Boltzmann constant, $\omega_{\mathcal{P}} = k_BT\sqrt{\mathcal{P}}/\hbar$, $\mathbf{R}_i^{(s)}$ are the ionic positions at imaginary time slice s, and $E[\{\phi_j\}^{(s)}, \{\mathbf{R}_i\}^{(s)}]$ is the KS energy functional of the KS orbitals ϕ_j and ionic positions, the evaluation of which includes the sum over ionic indices i and electronic indices j. For the XC part of the KS energy functional we use T-SCAN-L+rVV10. For a system with volume V, the pressure P is estimated with the following relation:

$$P = \frac{N\mathcal{P}k_BT}{V} - \frac{1}{3V}\sum_{s=1}^{\mathcal{P}}\sum_{i=1}^{N}\left[M\omega_{\mathcal{P}}^2\left(\mathbf{R}_i^{(s)} - \mathbf{R}_i^{(s+1)}\right)^2 + \frac{1}{\mathcal{P}}\mathbf{R}_i^{(s)}\cdot\frac{\partial E[\{\phi_j\}^{(s)}, \{\mathbf{R}_i\}^{(s)}]}{\partial \mathbf{R}_i^{(s)}}\right], \quad (5)$$

where all other symbols retain the same meaning as in Eqs. (3) and (4). In the limit of $\mathcal{P} = 1$ the classical Born-Oppenheimer molecular dynamics (BOMD) method is recovered [68,69] and in the limit of $\mathcal{P} \to \infty$, the classical ring-polymer system becomes isomorphic to the true quantum-ion one. Details about our calculations and convergence tests for the value of $\mathcal{P}$ necessary to approach the quantum limit within certain accuracy are discussed in Sec. III.

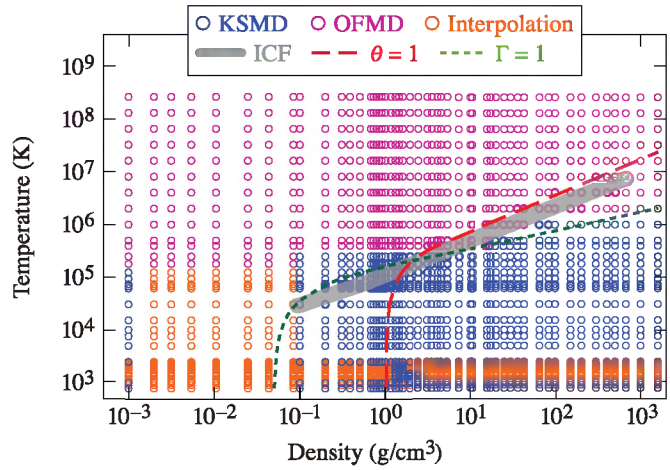

FIG. 2. Density-temperature points (circles) covered by iFPEOS, color-coded based on type of calculation: KSMD, blue; OFMD, purple; interpolation, orange. For reference, we plot some relevant plasma parameters: green line corresponds to dimensionless coupling parameter $\Gamma = 1$ and red line corresponds to degeneracy parameter $\Theta = 1$ for a partially ionized plasma, where the ionization fraction has been determined via Saha's equation by taking into account continuum lowering using the Stewart-Pyatt model [79]. Below the red and the green lines, which is mostly covered by KSMD, the system is strongly coupled and degenerate. Gray line shows the path of the imploding shell during ICF. The collection of KSMD points in the region around $\rho \sim 1.5$–2.5 g/cm^3, $T \sim 1000$–2500 K corresponds to the region of molecular dissociation, where we use extra-fine sampling in T space ($\Delta T = 100$ K) for an accurate description of the dissociation boundary.

III. BOMD COMPUTATIONAL DETAILS

iFPEOS includes 53 ρ points in the range of $0.001 \leqslant \rho \leqslant 1596.49$ g/cm^3 and 39 T points in the range $800\text{ K} \leqslant T \leqslant 256$ MK. Figure 2 shows all density-temperature points and the type of calculation corresponding to each one. AIMD calculations were performed in the NVT ensemble (number of particles, volume and temperature are kept constant) regulated by the Nosé-Hoover thermostat [70]. For KSMD we use the Vienna *ab initio* simulations package (VASP) [71,72] which is a plane-wave code that implements the projector-augmented wave (PAW) method [73,74]. The PAW method greatly simplifies the treatment of the electron-ion interaction by replacing the rapidly changing all-electron (AE) KS orbitals in the region near the nucleus with smooth nodeless pseudoorbitals (PS) (thereby drastically decreasing the required plane-wave energy cutoff) and then restoring the all-electron behavior and nodal structure by a linear transformation from the PS to the AE orbitals. This approximation breaks down, however, at high T and/or high ρ as nuclei come closer and closer together and augmentation spheres start to overlap. We have performed convergence tests with respect to

the augmentation sphere radius and, consequently, plane-wave energy cutoff, at different T and ρ conditions, ensuring that no accuracy greater than ~1% in both P and internal energy is sacrificed. We use two different PAW pseudopotentials (PP) with different augmentation sphere radii: $R_{\text{cut}} = 1.1$Å (soft) and $R_{\text{cut}} = 0.8$Å (hard), as well as a bare Coulomb potential. The soft PAW PP is accurate enough for the low-T, low-ρ regime, and as T and ρ increase, we find that the hard PAW PP and the bare Coulomb potential become necessary. The plane-wave energy cutoffs are 500, 1400, and 2100 eV for the soft, hard PAW PP and bare Coulomb potentials, respectively. All calculations were performed at the Baldereschi mean value point [75]. Convergence tests for simulation cell size, which in turn determines the number of particles in the box, and number of thermally occupied bands included in each simulation were also performed. All bands with occupation $\gtrsim 10^{-6}$ were included in each simulation. Initial geometries for the low-density, low-T regime, where the system is expected to be fully or partly molecular, were constructed by random placement of D_2 molecules and only the part of the MD simulation after the system has come to equilibrium was kept for analysis. In the regime where the system is fully atomic, simulations start from a random placement of D atoms. The time step for each ρ, T point was determined by performing a convergence test at certain conditions, $T' = 100$ K, $\rho' = 1.0$ g/cm^3, and scaling to other conditions via $t = (T'/T)^{(1/2)}(\rho'/\rho)^{(1/3)}$. We find that this scaling relation ensures that the average ion displacement remains uniform at all ρ and T conditions. T-SCAN-L was implemented into locally modified versions of the VASP and QUANTUM ESPRESSO codes by combining the previously implemented and extensively tested SCAN-L, KDT16 [22,24,26,50] [see Sec. II, Eq. (2)] and ground-state PBE (part of standard release). PIMD simulations were performed with the I-PI code [76], which is a Python interface for the quantum ion dynamics based on forces calculated by an external electronic structure code, in our case VASP. OFMD simulations are performed with the PROFESS@QUANTUM ESPRESSO package [14] and local pseudopotential [77].

KS calculations cover densities from $0.1 \leqslant \rho \leqslant 1596.49$ g/cm^3 and temperatures from 800 K up to 250 kK for the density range $0.1 \leqslant \rho \leqslant 15.71$ g/cm^3, and for higher densities we were able to perform KSMD for temperatures above 250 kK (see Fig. 2). For higher-T points KSMD becomes too computationally demanding, therefore, for those temperatures we use OFMD (see Fig. 2 and detailed explanation below). In addition to the high-T regime, the low-T, low-density ($\rho < 0.1$ g/cm^3) regime is also computationally challenging. Therefore, in the range $0.002 \leqslant \rho \leqslant 0.084$ g/cm^3, we perform OFMD calculations for $T \geqslant 182$ kK only. At these conditions we expect OFMD and KSMD results for pressure and energy to agree within 1%. This is further justified by performing KSMD and OFMD calculations along the lowest-density, $\rho = 0.001$ g/cm^3 isochore. Below $T = 182$ kK, however, OFMD becomes unreliable and KSMD becomes too computationally expensive. Therefore, in the range $0.002 \leqslant \rho \leqslant 0.084$ g/cm^3, 800 K $\leqslant T \leqslant$ 182 kK, we interpolate [78] using our results for the $\rho = 0.001$, 0.1, 0.2, and 0.3 g/cm^3 isochores from $T = 800$ K to $T = 500$ kK, and the $T = 182$, 250, 400, 500 kK isotherms from $\rho = 0.001$ g/cm^3 to $\rho = 0.3$ g/cm^3 (orange circles in lower left quadrant of Fig. 2). We advise cautious use of iFPEOS in this relatively large region of interpolation within which important processes such as molecular dissociation and ionization are encountered. Comparison between this region of interpolation and the well-established H-REOS.3 [13], which specifically targets this low-energy-density regime, as well as details of the KSMD calculations of the $\rho = 0.001$ g/cm^3 isochore are presented in the SM [36].

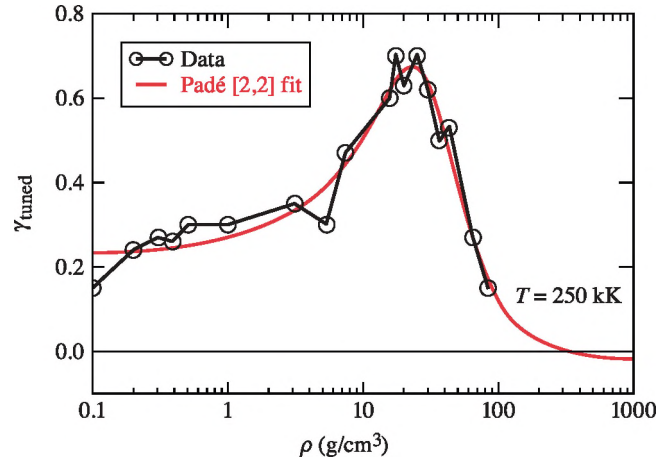

FIG. 3. A Padé [2,2] analytical fit (red curve) to the values of the γ parameter tuned to match KSMD results at select density points (black circles). The analytical fit provides the values of γ for OFMD calculations across entire iFPEOS density range.

OFMD calculations were carried out with recently introduced noninteracting free-energy density functional LKTFγTF (see Sec. II B) and T-SCAN-L free-energy density functional for the XC part of the electron-electron interaction (see Sec. II A). At such high T, the rVV10 correction is essentially zero, so the XC part in OFMD calculations is T-SCAN-L only. LKTFγTF is parametrized with respect to a reference KS calculation at certain ρ and T and transferred to higher T within the transferability domain. The standard procedure is as follows: (1) perform a KS calculation at certain ρ and T, which serves as reference; (2) perform OF calculations with LKTFγTF, varying γ to find the value that gives results for P that match the KS reference value; and (3) use this γ for all higher-T points along the isochore. Here, we tune the γ parameter to match KSMD results for P at the highest-T point for which we have a KS calculation. We find that tuning γ only at select density points and applying an analytical fit for γ's dependence on ρ is enough to parametrize γ across the entire table. The results for γ at the density points at which we perform explicit matching with KS results, along with the analytical fit (Padé approximant), are shown in Fig. 3.

The disagreement between the analytical fit and explicit calculations is mostly a result of statistical uncertainty in the MD runs; therefore, since the analytical fit serves as a de facto statistical averaging, we use γ provided by the analytical fit for all densities, even for those for which γ has been tuned explicitly. For $\rho \leqslant 0.1$ g/cm^3, we use $\gamma = 0.233$ and, for

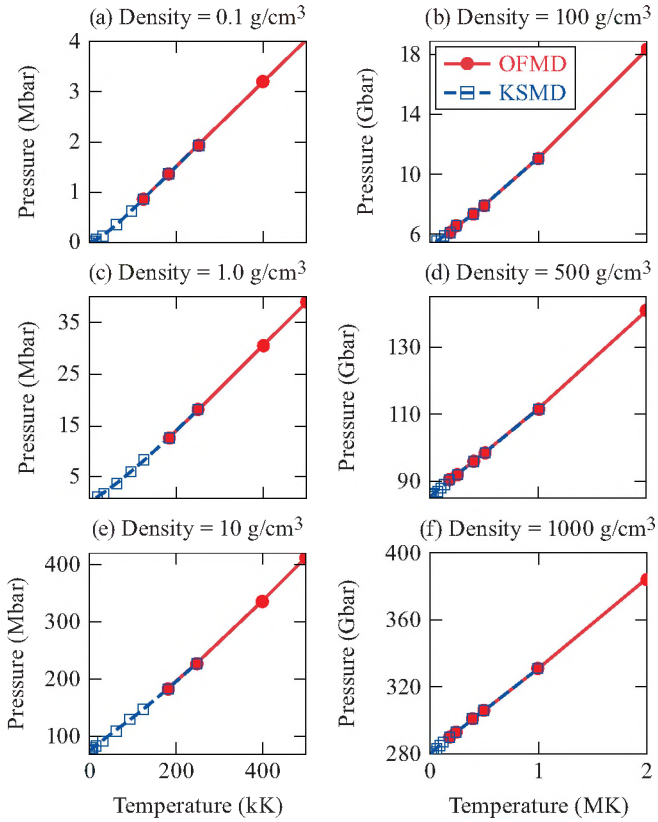

FIG. 4. Comparison between KSMD (blue squares) and OFMD (red circles) pressures along selected isochores that span iFPEOS. For each of the densities, γ was tuned with respect to the KS calculation at the highest-T point shown.

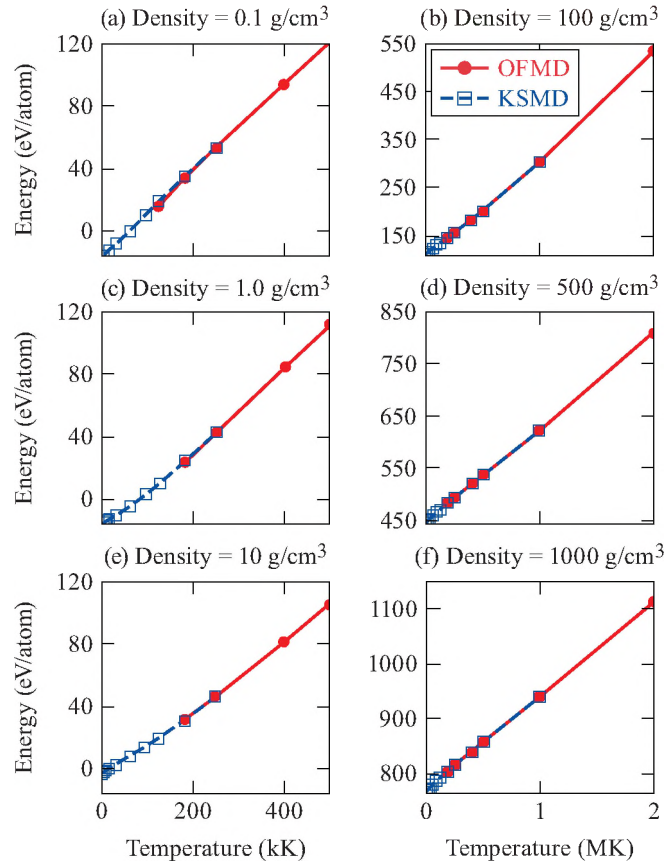

FIG. 5. Comparison between KSMD (blue squares) and OFMD total internal energies (red circles) along selected isochores that span iFPEOS. OFMD calculations have been performed with γ tuned at the highest-T KS calculation presented. OFMD energies at highest-T KSMD calculations have been shifted to match the KSMD energies, and the same shift has been applied to the lower-T points.

$\rho \geqslant 300$ g/cm^3, we use $\gamma = 0.0$. OFMD calculations were performed with PROFESS@QUANTUM ESPRESSO [14].

As explained in Ref. [44], the higher the T at which γ tuning is performed, the better the agreement between KS and OF calculations; therefore, here we tune γ at the highest-T points for which KS calculations were performed. To verify transferability to different T conditions, we performed additional OF calculations at the next few lower-T points along several isochores that span the range $0.1 \leqslant \rho \leqslant 1000$ g/cm^3 (see Fig. 4 for the excellent agreement between OFMD with LKTFγTF and KSMD for results for P).

Since we perform KS calculations with VASP, using a PAW data set, and OF calculations with PROFESS@QUANTUM ESPRESSO using local pseudopotentials, results for total internal energies are not compatible. This inconsistency is purely due to difference in computational procedures and can be remedied by either construction of pseudopotentials compatible with both codes or applying an energy shift. While the latter seems like a much simpler solution, the energy shift that needs to be applied, due to the approximate character of the noninteracting free-energy functional, depends on thermodynamic conditions and needs to be determined for every OFMD calculation. We find that this energy shift has a weak T dependence in the region where KSMD calculations switch to OFMD. Therefore, the magnitude of the energy shift is determined by the difference between the KSMD and the γ-tuned OFMD results for total energies at the highest-T point along each isochore. This density-dependent energy shift is assumed constant for higher temperatures. The excellent agreement between KSMD and OFMD energies for six isochores that span iFPEOS is illustrated in Fig. 5.

IV. NUCLEAR QUANTUM EFFECTS ON IFPEOS

PIMD calculations with quantum ions simulated by an N-bead ring polymer are N times more expensive than BOMD, which renders using PIMD for the entire iFPEOS prohibitively expensive. Here we find that for $N = 8$, pressure and energy have converged to within 1%. Therefore, we performed PIMD calculations at select density points in the region $0.3 \leqslant \rho \leqslant 1596.49$ g/cm^3 starting from the lowest $T = 800$ K point and going up in T along each isochore until NQEs vanish. In principle, BOMD performed with VASP and one-bead PIMD calculations with I-PI interfaced with VASP should give identical results; however, the two calculations give slightly different results mainly due to the difference in thermostats. The I-PI code utilizes the PILE-G stochastic thermostat [80]. Therefore, to eliminate this inconsistency, for each ρ-T point, we performed additional one-bead PIMD

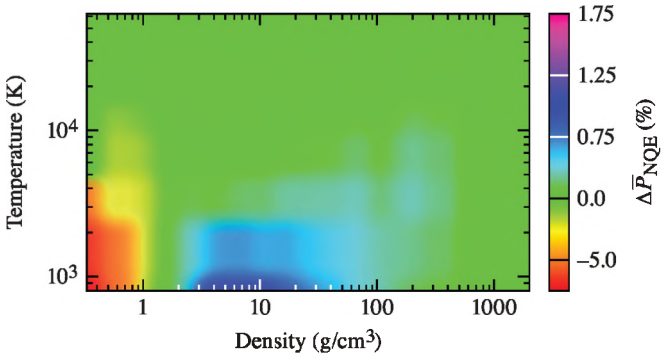

FIG. 6. Relative corrections to pressure as a function of T and ρ, $\Delta\overline{P}_{\rm NQE}(\rho, T)$ plotted in the ρ-T region of iFPEOS for which explicit PIMD calculations were performed. Note that, for clarity, below 0.0, the color gradient does not change linearly with change in $\Delta P_{\rm NQE}(\rho, T)$.

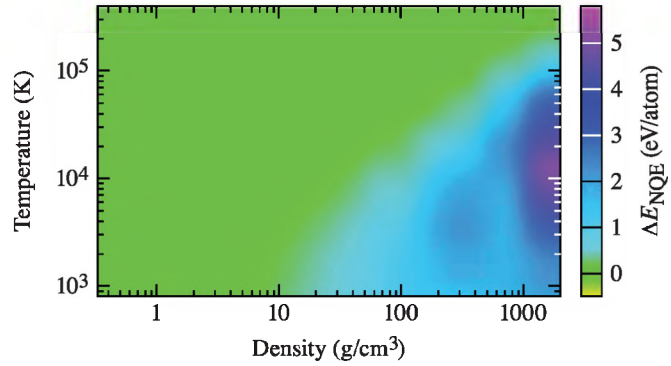

FIG. 7. Contour plot of the difference between PIMD and BOMD total internal energies.

(effectively, BOMD) as well as the eight-bead calculations, and the resulting differences in P and E between the two calculations are applied to the BOMD calculations as NQEs *corrections*. Figure 6 shows the relative correction to pressures due to NQEs, $\Delta\overline{P}_{\rm NQE}(\rho, T)$, defined as

$$\Delta\overline{P}_{\rm NQE}(\rho, T) = \frac{\Delta P_{\rm NQE}(\rho, T)}{P_{\rm BOMD}(\rho, T)} \times 100,$$
$$\Delta P_{\rm NQE}(\rho, T) = P_{\rm PIMD}(\rho, T) - P_{\rm BOMD}(\rho, T). \quad (6)$$

At high T, above ∼10 kK, NQEs corrections vanish. At low T we identify two distinct regions where NQEs corrections are significant ($\gtrsim$1%). Below ∼1 g/cm^3 PIMD calculations predict lower P than BOMD and above ∼2 g/cm^3 PIMD pressures are higher. This sign change in $\Delta\overline{P}_{\rm NQE}$ occurs around the molecular dissociation boundary. For $\rho \gtrsim 2$ g/cm^3, $T \sim 1$ kK (blue region in Fig. 6) where the system is atomic fluid, $\Delta\overline{P}_{\rm NQE}$ is positive, which is expected and was recently demonstrated by Kang *et al.* [34]. In the region of molecular D_2 ($\rho \leqslant 1$ g/cm^3), however, NQEs lower the pressure. This can be explained by the fact that NQEs tend to facilitate dissociation [21,81] and at this low-ρ regime, where the transition boundary is not well defined, PIMD could be predicting a higher fraction of atomic D and, therefore, lower pressures. This reasoning is further supported by results obtained by Caillabet *et al.* [21].

In the lower left corner of Fig. 6 ($\rho \leqslant 0.5$ g/cm^3, $T \leqslant 2500$ K) $\Delta\overline{P}_{\rm NQE}$ reaches values of $\sim -30\%$. This large relative difference between PIMD and BOMD is due to a sudden drop in total pressure [denominator on the right-hand side in Eq. (6)], as at these ρ-T conditions the degeneracy pressure diminishes. For densities lower than $\rho = 0.3$ g/cm^3, PIMD calculations become computationally expensive, and it is reasonable to assume that $\Delta\overline{P}_{\rm NQE}(\rho)_{T=800\ \rm K}$ remains approximately constant. The rationale behind this assumption is based on the fact that, since the degeneracy pressure no longer plays a major role, both $\Delta P_{\rm NQE}(\rho, T)$ and $P_{\rm BOMD}(\rho, T)$ continue decreasing at approximately the same rate. The NQEs corrections found at the higher-T points along the $\rho = 0.3$ g/cm^3 isochore were applied to corresponding T points at lower densities. $\Delta\overline{P}_{\rm NQE}(\rho, T)$ peaks in the region $4 \leqslant \rho \leqslant 10$ g/cm^3, $T = 800$ K and decreases for higher densities as a result of the much-faster-increasing total pressures compared to $\Delta P_{\rm NQE}(\rho, T)$.

NQEs corrections to total internal energies $\Delta E_{\rm NQE}(\rho, T) = E_{\rm PIMD}(\rho, T) - E_{\rm BOMD}(\rho, T)$ are shown in Fig. 7. For densities below ∼150 g/cm^3, NQEs corrections decrease monotonically as T rises. For $\rho \gtrsim 150$ g/cm^3, however, NQEs energy corrections increase with increasing T and a peak is observed at temperatures around 2 to 20 kK. A similar effect, although less pronounced, is observed in the NQEs corrections to total P. This nonmonotonic behavior of $\Delta E_{\rm NQE}$ and $\Delta P_{\rm NQE}$ is due to two competing effects: (1) NQEs decrease as T increases, and (2) NQEs increase as atoms get closer and closer together. The latter is amplified at high ρ and for $\rho \gtrsim 150$ g/cm^3, it dominates the low-T regime.

V. COMPARISON WITH EXPERIMENT AND OTHER MODELS

In the following section we aim to benchmark iFPEOS against some of the latest experimental measurements and compare to other EOS models based on different methodologies. One material property that can be directly measured in experiment and calculated from an EOS table is the Eulerian sound speed, which is defined as the square root of the rate of change of the pressure with respect to density at constant entropy:

$$c = \sqrt{\left(\frac{\partial p}{\partial \rho}\right)_S}. \quad (7)$$

Recent measurements by Fratanduono *et al.* [6] and Holmes [82] along with predictions by iFPEOS and other select models are shown in Fig. 8. iFPEOS (green curve in Fig. 8) is in excellent agreement with the experimental data by Holmes [82] in the low-P ($10 < P < 30$ GPa), low-ρ ($0.6 < \rho < 0.8$ g/cm^3) regime which coincides with the conditions for molecular dissociation. This agreement with experiment further verifies iFPEOS's accurate modeling of the molecular-to-atomic transition, even at low densities, where the transition is smooth (lower than those presented in Fig. 1, Sec. I). At higher pressures ($50 < P < 150$ GPa), we again see a good agreement between iFPEOS and experiment which is an improvement compared to other models, especially the

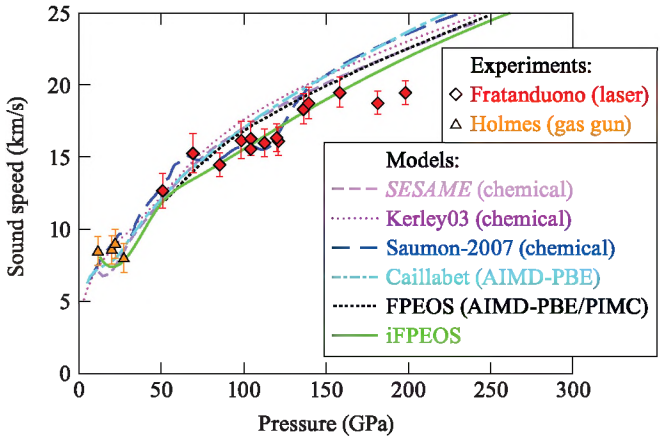

FIG. 8. Eulerian sound speed as a function of pressure in D along the principal Hugoniot. iFPEOS (green curve) is in good agreement with experimental measurements by Holmes [82] (orange triangles) and Fratanduono *et al.* [6] (red diamonds) for pressures up to ∼175 GPa.

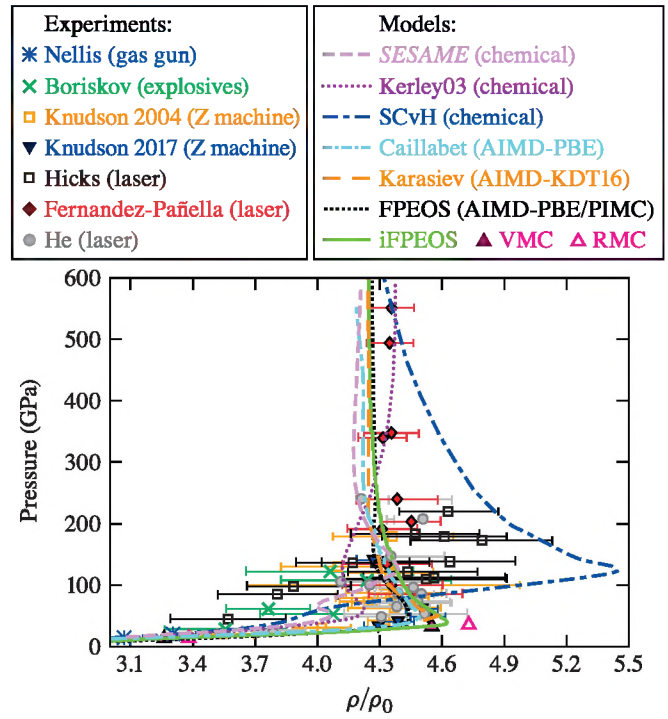

FIG. 9. Pressure as a function of density compression along the principal Hugoniot of D according to iFPEOS (green curve) compared to latest experimental measurements, various EOS models, and other Hugoniot calculations. Early gas gun measurements by Nellis *et al.* [88] at $P < 20$ GPa are blue stars. Shock compression by converging explosives by Boriskov *et al.* [86] (green crosses) is in good agreement with the chemical models SESAME [10] (light purple dashed line) and Kerley03 [9] (dark purple dotted line). Orange empty squares are magnetically driven flyer plate measurements [90] and black empty squares are laser-driven shock compression measurements [84]. High-precision Z-pinch measurements [85] (blue inverted triangles) are in good agreement with recent laser-driven shock compression (red diamonds [5] and gray filled circles [91]) in the low-ρ regime. Light blue dots and dashes are PBE-based EOS model by Caillabet *et al.* [21], black dotted line is FPEOS [11,19], orange dashes are Hugoniot calculations based on DFT with KDT16 thermal XC functional [22], and pink triangles are recent variational Monte Carlo (filled) and reptation Monte Carlo (empty) calculations [89]. iFPEOS is green, solid line.

PBE-based FPEOS and Caillabet which tend to overestimate c in this regime. This improvement can be explained by XC thermal effects which are expected to be important in this T regime ($10 \lesssim T \lesssim 80$ kK) [48] and are captured by T-SCAN-L, as well as the improved accuracy provided by SCAN-L over PBE. For $P > 180$ GPa, iFPEOS predicts ∼10% higher sound speed compared to experiment. This disagreement with experimental measurements at high P is characteristic not only to iFPEOS, but also to other models based on different methodologies such as PIMC and chemical models.

Another robust verification of the accuracy of a theoretical EOS model can be done by comparing the model's prediction of the principal Hugoniot with that measured in experiment. When a liquid is shock compressed, the internal energy per unit mass E, the pressure P, and the density ρ behind the shock front are related to those in front of it (E_0, P_0, ρ_0) through the following equation:

$$E - E_0 = \frac{1}{2}(P + P_0)\left(\frac{1}{\rho_0} - \frac{1}{\rho}\right), \tag{8}$$

known as the Rankine-Hugoniot (RH) equation [83] and in single-shock compression from ambient conditions the thermodynamic states satisfying Eq. (8) form the principal Hugoniot. The D principal Hugoniot has been extensively studied experimentally [5,84–88] and theoretically [9,10,21,22,89]. The principal Hugoniot in P-compression space (Fig. 9) and in T-compression space (Fig. 10) is compared below to popular first-principles and chemical-model-based EOS table and latest experimental measurements obtained with various techniques.

In order to obtain a more-systematic comparison with experiment, we determine P_0 and E_0 in Eq. (8) with an additional calculation at the initial conditions: $\rho_0 = 0.173$ g/cm^3 and $T_0 = 19$ K, which are the initial conditions reported by Fernandez-Pañella *et al.* [5]. These initial conditions were chosen so that iFPEOS can be compared to the latest experimental measurements which also probe the high-P, high-T regime. Computations at such low T_0 and ρ_0 are challenging because the uncertainty in P_0 calculated with the largest unit cell achievable with our methods is larger by approximately two orders of magnitude than the extremely low value for P_0 (∼10^{-4} GPa), therefore, we take $P_0 = 0.0$ GPa. We tested the effect of P_0 on the Hugoniot and for $0 < P_0 < 10^{-2}$ GPa, we see a maximum variation in the predicted compression of less than 0.01%. For initial energy we obtain $E_0 = -15.7755 \pm 0.0004$ eV/atom. To verify the accuracy of our value for E_0, we perform an additional calculation on an isolated D_2 molecule and compare to high-precision wave-function-based calculations [96]. Our result $E_{D_2} = -15.8192 \pm 0.0002$ eV/atom is only 0.4% higher than the reported value; $E_{D_2} = -15.886$ eV/atom. To obtain the principal Hugoniot with higher accuracy, we increase the density point sampling around the anticipated region of maximum compression and high-pressure Hugoniot, which occur

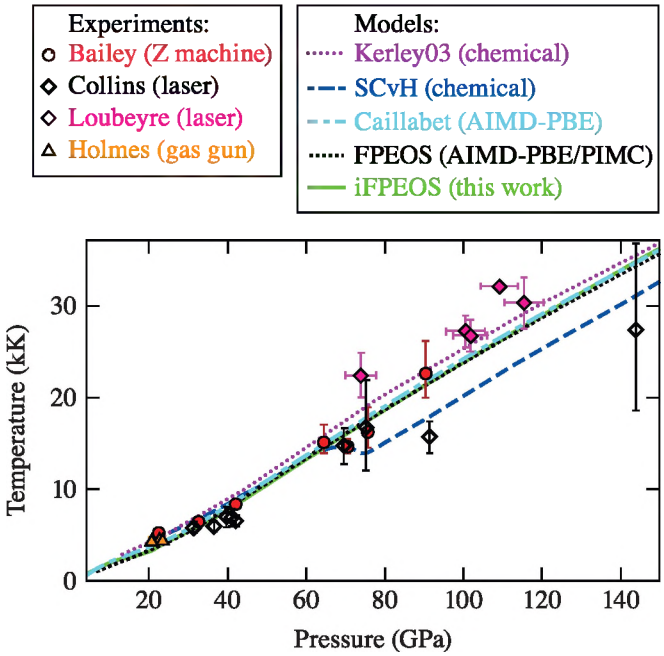

FIG. 10. Temperature as a function of pressure along the principal Hugoniot. Experimental results are shown as yellow triangles (gas gun) [92], black empty diamonds (laser) [93], magenta diamonds (laser) [94], and brown filled circles (Z machine) [95]. Theoretical models are labeled as in Figs. 8 and 9.

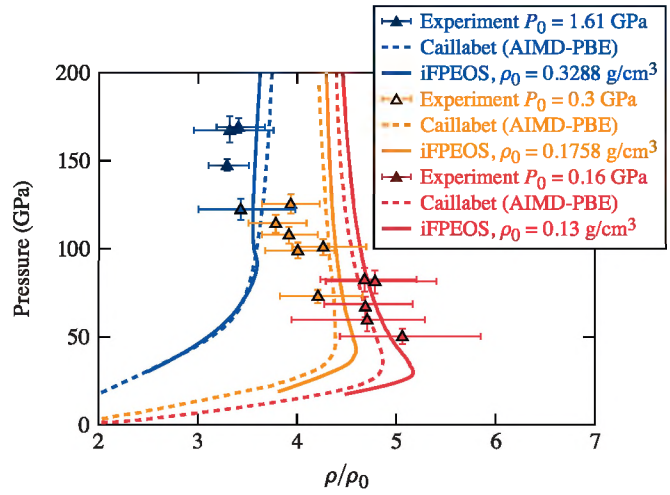

FIG. 11. Shock Hugoniot for different precompressed D_2 samples at $T = 297$ K. Red: $\rho_0 = 0.13$ g/cm^3, $P_0 = 0.16$ GPa; orange: $\rho_0 = 0.1758$ g/cm^3, $P_0 = 0.3$ GPa; blue: $\rho_0 = 0.3288$ g/cm^3, $P_0 = 1.6$ GPa. Triangles: experimental measurements [94]; dashed curves: AIMD calculations with PBE XC [21]; solid curves: iFPEOS.

in the range $0.6 \lesssim \rho \lesssim 0.8$ g/cm^3. The smooth Hugoniot curve shown in Fig. 9 has been obtained by solving the RH equations on a dense ρ-T grid ($\Delta\rho = 0.0005$ g/cm^3, $\Delta T = 250$ K) obtained through spline interpolation [78] applied to the ρ-T points corresponding to explicit calculations shown in Fig. 2. Here we note that the maximum compression peak in the iFPEOS principal Hugoniot at $\rho/\rho_0 = 4.64$ corresponds to $T = 8000$ K, which is close to the 7500-K isotherm for which we have performed explicit KSMD calculations and, therefore, any potential error in the maximum compression peak due to interpolation has been eliminated. According to iFPEOS, maximum compression is 2.5% higher than the highest-compression experimental datum by Knudson *et al.* [85] and the maximum compression predicted by the KDT16 thermal functional [22] and 3.5% higher than the PBE prediction. In addition, the iFPEOS maximum compression is halfway between recent high-precision variational Monte Carlo (VMC) (1.9% lower than iFPEOS) and reptation Monte Carlo (RMC) (1.8% higher than iFPEOS) calculations in this regime. In the region immediately above maximum compression, $P \sim 100$ GPa, iFPEOS is in excellent agreement with recent experimental measurements by Fernandez-Pañella *et al.* [5]. For $P > 200$ GPa, however, iFPEOS predicts a significantly stiffer ($\sim$1.5%) Hugoniot compared to experiment, consistent with PIMC and KDT16-based predictions in this regime. Comparison between iFPEOS with other popular models and experimental measurement of T and P along the principal Hugoniot (Fig. 10) shows that there is an excellent agreement between the first-principles models up to $P = 150$ GPa, however, the growing disagreement between theoretical models and experiments as pressure grows is evident.

We also compare iFPEOS with experimental measurements of shock Hugoniot data from laser-driven shock compression of D_2 targets, precompressed to different initial pressures, as reported by Loubeyre *et al.* [94], where diamond anvil cell is used to precisely control the initial density of the sample. Measurements of Hugoniot data are reported for five shots at initial pressure $P_0 = 0.16 \pm 0.03$ GPa ($\rho_0 = 0.13 \pm 0.012$ g/cm^3), six shots at $P_0 = 0.3 \pm 0.03$ GPa, and four shots at $P_0 = 1.61 \pm 0.03$ GPa. To compare iFPEOS with those measurements, we performed extra calculations at the reported initial conditions: $T = 297$ K, $\rho_0 = 0.13$, 0.1758, and 0.3288 g/cm^3. The iFPEOS Hugoniot curve for each ρ_0 are compared to experimental measurements and a PBE-based model [21] in Fig. 11. For the lowest initial density $\rho = 0.13$ g/cm^3, iFPEOS predicts a softer Hugoniot compared to PBE, consistent with results for principal Hugoniot, and $\sim$6% higher maximum compression which is in much better agreement with highest-compression experimental datum. At these conditions, improved accuracy is attributed to the advanced, meta-GGA level of XC treatment. The $\rho_0 = 0.1758$ g/cm^3 precompressed Hugoniot is similar to the principal Hugoniot shown in Fig. 9 for which $\rho_0 = 0.173$ g/cm^3. At these initial conditions the iFPEOS Hugoniot curve moves closer to the PBE one, however both are at significantly higher compression than the majority of experimental data points. Finally, for the case of $\rho_0 = 0.3288$ g/cm^3 we find that iFPEOS and PBE Hugoniot curves are in agreement up to $P \sim 100$ GPa. At higher pressures $T \gtrsim 10\,000$ K, which is the temperature regime in which XC thermal effects become important and are the reason for the Hugoniot hardening towards the experimental data points at $\rho/\rho_0 \sim 3.3$.

Next, we compare iFPEOS with experimental measurements of reshock Hugoniot data. The pressure in the reshocked deuterium is determined by impedance matching with the standard, in the case of latest measurements by

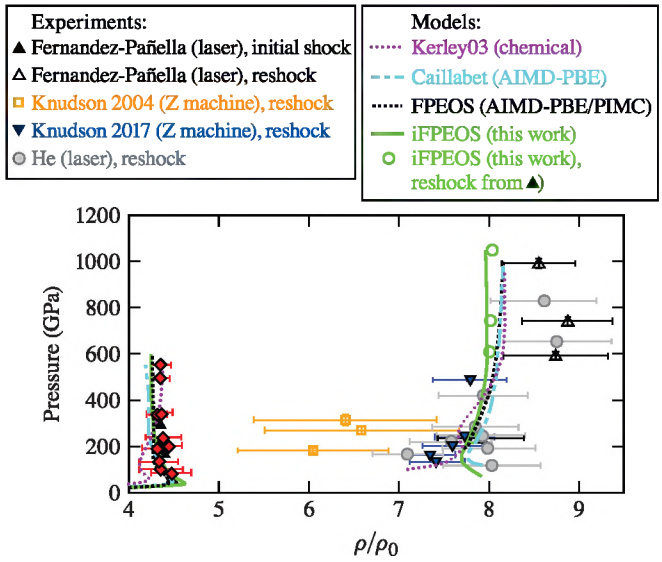

FIG. 12. Single and reflected shock states in D. Figures in the lower left corner correspond to principal Hugoniot figures in Fig. 9. Model labels match those from Figs. 8, 9, and 10. All experimental reflected shocks are from an α-quartz standard. Black filled triangles are initial states in the shocked D prior to reflection and black empty triangles are the corresponding reshock states. Green open circles correspond to iFPEOS prediction of reshock states launched from the initial states reported in [5]. Green solid curve corresponds to the iFPEOS reshock launched from the iFPEOS principal Hugoniot using impedance matching with the α-quartz. Experimental secondary-shock data using magnetically driven flyer plates are orange open squares [90] and blue inverted triangles [85], and using laser-driven shock compression are gray filled circles [91].

Fernandez-Pañella [5], α-quartz, in a manner consistent with that described in the SM in Ref. [5]. In brief, one solves the RH jump relation, which is Eq. (8) in combination with the following:

$$\rho = \frac{\rho_0 (U_s - U_{p_0})}{U_s - U_p}, \tag{9}$$

$$P = P_0 + \rho_0 (U_s - U_{p_0})(U_p - U_{p_0}) \tag{10}$$

for given measured shock velocity U_s and initial particle velocity U_{p_0}. The reshock Hugoniot in pressure-particle velocity (P-U_p) space is launched off of the same initial state as that reported in experiment and its intersection with the α-quartz principal Hugoniot determines the final P in the reshocked D. These final pressures determine the states on each reshock Hugoniot in pressure-compression space launched from the initial states reported in experiment (black, filled triangles in Fig. 12) and are reported as green circles in Fig. 12. We also show the reshock Hugoniot using the iFPEOS principal Hugoniot as initial conditions (green curve in Fig. 12) and not the experimentally determined initial states, which is a more self-consistent prediction and allows for a more direct comparison with other experimental measurements. As in the case of principal Hugoniot, iFPEOS reshock states are in good agreement with experiment and other first-principles models in the low-P regime around 200 GPa, but significantly underestimate the compression (6%–11%) for the three data points above 600 GPa, thereby confirming a systematic disagreement between theory and experiment in this high-P regime.

VI. SUMMARY

We have presented iFPEOS, an EOS table of deuterium which includes major developments in the AIMD methodology, such as a more accurate XC functional, proper treatment XC thermal effects, and quantum treatment of ions. iFPEOS employs the newly developed T-SCAN-L XC functional, which is at the more-accurate meta-GGA level of DFT and accounts for XC thermal effects. Long-range van der Waals interactions are taken into account by combining T-SCAN-L with the rVV10 functional. Finally, iFPEOS takes into account NQEs via PIMD calculations.

iFPEOS reports pressures and internal energies for densities $0.001 \leqslant \rho \leqslant 1596.46$ g/cm^3 and temperatures 800 K $\leqslant T \leqslant 256$ MK. Conditions in which the system is strongly coupled and degenerate are almost entirely covered by KSMD. DFT calculations in the high-T regime ($T >$ 250 000 K) have been made possible with the newly developed LKTFγTF OF DFT functional, which greatly reduces the computational cost without introducing thermodynamic inconsistencies.

Results are compared with latest experimental measurements and other popular models' predictions of the properties of D at a wide range of pressures and temperatures. We conclude that iFPEOS is expected to provide an improved description of D for $T \lesssim 60\,000$ K, $P \lesssim 200$ GPa based on our results of sound speed and the molecular dissociation boundary, where we see a clear improvement with the latest experimental data. This improvement can clearly be attributed to the advanced (meta-GGA level of DFT), thermal XC functional T-SCAN-L+rVV10, as it occurs precisely in conditions in which XC thermal effects (not included in PBE) and accurate prediction of D-D interaction energies are important. At higher pressures, however, iFPEOS predicts significantly higher sound speed, in agreement with other first-principles-based models. In the high-pressure regime of the principal Hugoniot iFPEOS predicts a significantly lower compression (~1.5%) than experimental measurements. However, we find that iFPEOS does provide ~1%–1.5% better agreement with experiment compared to PBE-based results and is in excellent agreement with PIMC-based results in that regime. A similar trend is seen in comparing iFPEOS with latest reshock measurements. At $P \sim 200$ GPa, iFPEOS, as well as other models, show excellent agreement with experiment. At $P > 600$ GPa, however, disagreement in predicted (by all models) and measured compression in the reshock state grows to 6%–11%. In summary, we have presented iFPEOS, an updated D EOS table which provides three important improvements to previous first-principles-based models: (1) an advanced, meta-GGA-level treatment of the XC interaction, (2) fully consistent treatment of XC thermal effects across all temperature conditions, and (3) quantum treatment of ions. Comparison with other models and latest experimental measurements show that iFPEOS does provide an improvement in accuracy where XC thermal effects are important and in the region of molecular dissociation. Finally, we conclude that the improved DFT methodology provided in iFPEOS does

not seem to resolve the long-standing disagreement between theory and experiment in the pressure regime above 200 GPa.

ACKNOWLEDGMENTS

This material is based upon work supported by the Department of Energy National Nuclear Security Administration under Award No. DE-NA0003856, U.S. National Science Foundation PHY Grant No. 1802964, the University of Rochester, and the New York State Energy Research and Development Authority. V.V.K. used resources of the National Energy Research Scientific Computing Center, a DOE Office of Science User Facility supported by the Office of Science of the U.S. Department of Energy under Contract No. DE-AC02-05CH11231. This paper was prepared as an account of work sponsored by an agency of the U.S. Government. Neither the U.S. Government nor any agency thereof, nor any of their employees, makes any warranty, express or implied, or assumes any legal liability or responsibility for the accuracy, completeness, or usefulness of any information, apparatus, product, or process disclosed, or represents that its use would not infringe privately owned rights. The views and opinions of authors expressed herein do not necessarily state or reflect those of the U.S. Government or any agency thereof.

[1] S. X. Hu, B. Militzer, V. N. Goncharov, and S. Skupsky, Strong Coupling and Degeneracy Effects in Inertial Confinement Fusion Implosions, Phys. Rev. Lett. **104**, 235003 (2010).

[2] V. N. Goncharov, O. V. Gotchev, E. Vianello, T. R. Boehly, J. P. Knauer, P. W. McKenty, P. B. Radha, S. P. Regan, T. C. Sangster, S. Skupsky *et al.*, Early stage of implosion in inertial confinement fusion: Shock timing and perturbation evolution, Phys. Plasmas **13**, 012702 (2006).

[3] B. A. Hammel, S. W. Haan, D. S. Clark, M. J. Edwards, S. H. Langer, M. M. Marinak, M. V. Patel, J. D. Salmonson, and H. A. Scott, High-mode Rayleigh-Taylor growth in NIF ignition capsules, High Energy Density Phys. **6**, 171 (2010).

[4] J. M. McMahon, M. A. Morales, C. Pierleoni, and D. M. Ceperley, The properties of hydrogen and helium under extreme conditions, Rev. Mod. Phys. **84**, 1607 (2012).

[5] A. Fernandez-Pañella, M. Millot, D. E. Fratanduono, M. P. Desjarlais, S. Hamel, M. C. Marshall, D. J. Erskine, P. A. Sterne, S. Haan, T. R. Boehly, G. W. Collins, J. H. Eggert, and P. M. Celliers, Shock Compression of Liquid Deuterium up to 1 TPa, Phys. Rev. Lett. **122**, 255702 (2019).

[6] D. E. Fratanduono, M. Millot, A. Fernandez Pañella, P. A. Sterne, G. W. Collins, D. G. Hicks, J. H. Eggert, T. R. Boehly, and P. M. Celliers, Measurement of the sound speed in dense fluid deuterium along the cryogenic liquid Hugoniot, Phys. Plasmas **26**, 012710 (2019).

[7] P. M. Celliers, M. Millot, S. Brygoo, R. S. McWilliams, D. E. Fratanduono, J. R. Rygg, A. F. Goncharov, P. Loubeyre, J. H. Eggert, J. L. Peterson *et al.*, Insulator-metal transition in dense fluid deuterium, Science **361**, 677 (2018).

[8] J. A. Gaffney, S. X. Hu, P. Arnault, A. Becker, L. X. Benedict, T. R. Boehly, P. M. Celliers, D. M. Ceperley, O. Čertík, J. Clérouin *et al.*, A review of equation-of-state models for inertial confinement fusion materials, High Energy Density Phys. **28**, 7 (2018).

[9] G. I. Kerley, Equations of state for hydrogen and deuterium, Sandia National Laboratories Technical Report, doi:10.2172/917468.

[10] D. Saumon, The SESAME 5267 equation of state of deuterium, Technical Report LA-UR-13-20032, Los Alamos National Laboratory, 2013.

[11] S. X. Hu, B. Militzer, V. N. Goncharov, and S. Skupsky, First-principles equation-of-state table of deuterium for inertial confinement fusion applications, Phys. Rev. B **84**, 224109 (2011).

[12] A. A. Correa, L. X. Benedict, M. A. Morales, P. A. Sterne, J. I. Castor, and E. Schwegler, A first-principles global multiphase equation of state for hydrogen, arXiv:1806.01346.

[13] A. Becker, W. Lorenzen, J. J. Fortney, N. Nettelmann, M. Schöttler, and R. Redmer, *Ab initio* equations of state for hydrogen (H-REOS.3) and helium (He-REOS. 3) and their implications for the interior of brown dwarfs, Astrophys. J. Suppl. Ser. **215**, 21 (2014).

[14] V. V. Karasiev, T. Sjostrom, and S. B. Trickey, Finite-temperature orbital-free DFT molecular dynamics: Coupling PROFESS and QUANTUM ESPRESSO, Comput. Phys. Commun. **185**, 3240 (2014).

[15] V. V. Karasiev, D. Chakraborty, O. A. Shukruto, and S. B. Trickey, Nonempirical generalized gradient approximation free-energy functional for orbital-free simulations, Phys. Rev. B **88**, 161108(R) (2013).

[16] J.-F. Danel, L. Kazandjian, and R. Piron, Equation of state of warm dense deuterium and its isotopes from density-functional theory molecular dynamics, Phys. Rev. E **93**, 043210 (2016).

[17] D. Saumon, G. Chabrier, and H. M. van Horn, An equation of state for low-mass stars and giant planets, Astrophys. J. Suppl. Ser. **99**, 713 (1995).

[18] G. Chabrier, S. Mazevet, and F. Soubiran, A new equation of state for dense hydrogen-helium mixtures, Astrophys. J. **872**, 51 (2019).

[19] S. X. Hu, V. N. Goncharov, T. Boehly, R. McCrory, S. Skupsky, L. A. Collins, J. D. Kress, and B. Militzer, Impact of first-principles properties of deuterium–tritium on inertial confinement fusion target designs, Phys. Plasmas **22**, 056304 (2015).

[20] B. Militzer, F. González-Cataldo, S. Zhang, K. P. Driver, and F. Soubiran, First-principles equation of state database for warm dense matter computation, Phys. Rev. E **103**, 013203 (2021).

[21] L. Caillabet, S. Mazevet, and P. Loubeyre, Multiphase equation of state of hydrogen from *ab initio* calculations in the range 0.2 to 5 g/cc up to 10 eV, Phys. Rev. B **83**, 094101 (2011).

[22] V. V. Karasiev, S. X. Hu, M. Zaghoo, and T. R. Boehly, Exchange-correlation thermal effects in shocked deuterium: Softening the principal Hugoniot and thermophysical properties, Phys. Rev. B **99**, 214110 (2019).

[23] V. V. Karasiev, J. W. Dufty, and S. B. Trickey, Nonempirical Semilocal Free-Energy Density Functional for Matter Under Extreme Conditions, Phys. Rev. Lett. **120**, 076401 (2018).

[24] J. Hinz, V. V. Karasiev, S. X. Hu, M. Zaghoo, D. Mejía-Rodríguez, S. B. Trickey, and L. Calderín, Fully consistent

density functional theory determination of the insulator-metal transition boundary in warm dense hydrogen, Phys. Rev. Res. **2**, 032065(R) (2020).

[25] D. Marx and M. Parrinello, *Ab initio* path integral molecular dynamics: Basic ideas, J. Chem. Phys. **104**, 4077 (1996).

[26] D. Mejia-Rodriguez and S. B. Trickey, Deorbitalization strategies for meta-generalized-gradient-approximation exchange-correlation functionals, Phys. Rev. A **96**, 052512 (2017).

[27] O. A. Vydrov and T. Van Voorhis, Nonlocal Van Der Waals Density Functional Made Simple, Phys. Rev. Lett. **103**, 063004 (2009).

[28] J. Sun, A. Ruzsinszky, and J. P. Perdew, Strongly Constrained and Appropriately Normed Semilocal Density Functional, Phys. Rev. Lett. **115**, 036402 (2015).

[29] H. Peng, Z.-H. Yang, J. P. Perdew, and J. Sun, Versatile Van Der Waals Density Functional Based on a Meta-Generalized Gradient Approximation, Phys. Rev. X **6**, 041005 (2016).

[30] R. C. Clay, III, M. Holzmann, D. M. Ceperley, and M. A. Morales, Benchmarking density functionals for hydrogen-helium mixtures with quantum Monte Carlo: Energetics, pressures, and forces, Phys. Rev. B **93**, 035121 (2016).

[31] M. A. Morales, J. M. McMahon, C. Pierleoni, and D. M. Ceperley, Nuclear Quantum Effects and Nonlocal Exchange-Correlation Functionals Applied to Liquid Hydrogen at High Pressure, Phys. Rev. Lett. **110**, 065702 (2013).

[32] M. Zaghoo, R. J. Husband, and I. F. Silvera, Striking isotope effect on the metallization phase lines of liquid hydrogen and deuterium, Phys. Rev. B **98**, 104102 (2018).

[33] J. Chen, X.-Z. Li, Q. Zhang, M. I. J. Probert, C. J. Pickard, R. J. Needs, A. Michaelides, and E. Wang, Quantum simulation of low-temperature metallic liquid hydrogen, Nat. Commun. **4**, 2064 (2013).

[34] D. Kang, K. Luo, K. Runge, and S. B. Trickey, Two-temperature warm dense hydrogen as a test of quantum protons driven by orbital-free density functional theory electronic forces, Matter Radiat. Extremes **5**, 064403 (2020).

[35] M. D. Knudson, M. P. Desjarlais, A. Becker, R. W. Lemke, K. Cochrane, M. E. Savage, D. E. Bliss, T. Mattsson, and R. Redmer, Direct observation of an abrupt insulator-to-metal transition in dense liquid deuterium, Science **348**, 1455 (2015).

[36] See Supplemental Material at http://link.aps.org/supplemental/10.1103/PhysRevB.xx.xxxxxx for the full iFPEOS table as well as details about calculations in the challenging low-density regime. See also for the full iFPEOS table as well as details about calculations in the challenging low-density regime.

[37] W. Kohn and L. J. Sham, Self-consistent equations including exchange and correlation effects, Phys. Rev. **140**, A1133 (1965).

[38] N. D. Mermin, Thermal properties of the inhomogeneous electron gas, Phys. Rev. **137**, A1441 (1965).

[39] M. V. Stoitsov and I. Z. Petkov, Density functional theory at finite temperatures, Ann. Phys. **184**, 121 (1988).

[40] R. Car and M. Parrinello, Unified Approach for Molecular Dynamics and Density-Functional Theory, Phys. Rev. Lett. **55**, 2471 (1985).

[41] R. N. Barnett and U. Landman, Born-oppenheimer molecular-dynamics simulations of finite systems: Structure and dynamics of (h 2 o) 2, Phys. Rev. B **48**, 2081 (1993).

[42] D. Marx and J. Hutter, in *Modern Methods and Algorithms of Quantum Chemistry*, edited by J. Grotendorst (John von Neumann Inst. for Computing, Jülich, 2000), Vol. 301.

[43] V. V. Karasiev, D. I. Mihaylov, and S. X. Hu, Meta-GGA exchange-correlation free-energy density functional to achieve unprecedented accuracy for warm-dense-matter simulations, Phys. Rev. Lett. (submitted).

[44] V. V. Karasiev, J. Hinz, and D. I. Mihaylov, Tunable non-interacting free-energy functionals (unpublished).

[45] A. Pribram-Jones, S. Pittalis, E. Gross, and K. Burke, Thermal density functional theory in context, in *Frontiers and Challenges in Warm Dense Matter* (Springer, Berlin, 2014), pp. 25–60.

[46] K. Burke, J. C. Smith, P. E. Grabowski, and A. Pribram-Jones, Exact conditions on the temperature dependence of density functionals, Phys. Rev. B **93**, 195132 (2016).

[47] J. C. Smith, A. Pribram-Jones, and K. Burke, Exact thermal density functional theory for a model system: Correlation components and accuracy of the zero-temperature exchange-correlation approximation, Phys. Rev. B **93**, 245131 (2016).

[48] V. V. Karasiev, L. Calderín, and S. B. Trickey, Importance of finite-temperature exchange correlation for warm dense matter calculations, Phys. Rev. E **93**, 063207 (2016).

[49] V. V. Karasiev, T. Sjostrom, J. Dufty, and S. B. Trickey, Accurate Homogeneous Electron Gas Exchange-Correlation Free Energy for Local Spin-Density Calculations, Phys. Rev. Lett. **112**, 076403 (2014).

[50] D. I. Mihaylov, V. V. Karasiev, and S. X. Hu, Thermal hybrid exchange-correlation density functional for improving the description of warm dense matter, Phys. Rev. B **101**, 245141 (2020).

[51] V. V. Karasiev, S. B. Trickey, and J. W. Dufty, Status of free-energy representations for the homogeneous electron gas, Phys. Rev. B **99**, 195134 (2019).

[52] B. Militzer, Path integral monte carlo and density functional molecular dynamics simulations of hot, dense helium, Phys. Rev. B **79**, 155105 (2009).

[53] L. H. Thomas, The calculation of atomic fields, in *Mathematical Proceedings of the Cambridge Philosophical Society*, (Cambridge University Press, Cambridge, 1927), Vol. 23, pp. 542–548.

[54] E. Fermi, Application of statistical gas methods to electronic systems, Atti R. Accad. Naz. Lincei Mem. Cl. Sci. Fis. Mat. Nat. **6**, 602 (1927).

[55] E. V. Ludeña and V. V. Karasiev, Kinetic energy functionals: history, challenges and prospects, in *Reviews of Modern Quantum Chemistry: A Celebration of the Contributions of Robert Parr*, edited by K. D. Sen (World Scientific, Singapore, 2002), pp. 612–665.

[56] K. Luo, V. V. Karasiev, and S. B. Trickey, A simple generalized gradient approximation for the noninteracting kinetic energy density functional, Phys. Rev. B **98**, 041111(R) (2018).

[57] R. P. Feynman, N. Metropolis, and E. Teller, Equations of state of elements based on the generalized Fermi-Thomas theory, Phys. Rev. **75**, 1561 (1949).

[58] F. Perrot, Gradient correction to the statistical electronic free energy at nonzero temperatures: Application to equation-of-state calculations, Phys. Rev. A **20**, 586 (1979).

[59] V. V. Karasiev, T. Sjostrom, and S. B. Trickey, Generalized-gradient-approximation noninteracting free-energy functionals

for orbital-free density functional calculations, Phys. Rev. B **86**, 115101 (2012).

[60] K. Luo, V. V. Karasiev, and S. B. Trickey, Towards accurate orbital-free simulations: A generalized gradient approximation for the noninteracting free energy density functional, Phys. Rev. B **101**, 075116 (2020).

[61] R. P. Feynman, A. R. Hibbs, and D. F. Styer, *Quantum Mechanics and Path Integrals* (Dover, New York, 2010).

[62] D. Chandler and P. G. Wolynes, Exploiting the isomorphism between quantum theory and classical statistical mechanics of polyatomic fluids, J. Chem. Phys. **74**, 4078 (1981).

[63] M. Suzuki, Fractal decomposition of exponential operators with applications to many-body theories and monte carlo simulations, Phys. Lett. A **146**, 319 (1990).

[64] M. E. Tuckerman, D. Marx, M. L. Klein, and M. Parrinello, Efficient and general algorithms for path integral Car–Parrinello molecular dynamics, J. Chem. Phys. **104**, 5579 (1996).

[65] I. R. Craig and D. E. Manolopoulos, Quantum statistics and classical mechanics: Real time correlation functions from ring polymer molecular dynamics, J. Chem. Phys. **121**, 3368 (2004).

[66] A. Pérez, M. E. Tuckerman, and M. H. Müser, A comparative study of the centroid and ring-polymer molecular dynamics methods for approximating quantum time correlation functions from path integrals, J. Chem. Phys. **130**, 184105 (2009).

[67] M. Rossi, M. Ceriotti, and D. E. Manolopoulos, How to remove the spurious resonances from ring polymer molecular dynamics, J. Chem. Phys. **140**, 234116 (2014).

[68] J. S. Tse, *Ab initio* molecular dynamics with density functional theory, Annu. Rev. Phys. Chem. **53**, 249 (2002).

[69] D. Marx and J. Hutter, *Ab initio Molecular Dynamics: Basic Theory and Advanced Methods* (Cambridge University Press, Cambridge, 2009).

[70] W. G. Hoover, Canonical dynamics: Equilibrium phase-space distributions, Phys. Rev. A **31**, 1695 (1985).

[71] G. Kresse and J. Furthmüller, Efficient iterative schemes for *ab initio* total-energy calculations using a plane-wave basis set, Phys. Rev. B **54**, 11169 (1996).

[72] G. Kresse and J. Furthmüller, Efficiency of *ab-initio* total energy calculations for metals and semiconductors using a plane-wave basis set, Comput. Mater. Sci. **6**, 15 (1996).

[73] P. E. Blöchl, Projector augmented-wave method, Phys. Rev. B **50**, 17953 (1994).

[74] G. Kresse and D. Joubert, From ultrasoft pseudopotentials to the projector augmented-wave method, Phys. Rev. B **59**, 1758 (1999).

[75] A. Baldereschi, Mean-value point in the Brillouin zone, Phys. Rev. B **7**, 5212 (1973).

[76] V. Kapil, M. Rossi, O. Marsalek, R. Petraglia, Y. Litman, T. Spura, B. Cheng, A. Cuzzocrea, R. H. Meißner, D. M. Wilkins *et al.*, i-PI 2.0: A universal force engine for advanced molecular simulations, Comput. Phys. Commun. **236**, 214 (2019).

[77] V. V. Karasiev and S. B. Trickey, Issues and challenges in orbital-free density functional calculations, Comput. Phys. Commun. **183**, 2519 (2012).

[78] H. Akima, A method of bivariate interpolation and smooth surface fitting for irregularly distributed data points, ACM Trans. Math. Software **4**, 148 (1978).

[79] B. J. B. Crowley, Continuum lowering–a new perspective, High Energy Density Phys. **13**, 84 (2014).

[80] M. Ceriotti, M. Parrinello, T. E. Markland, and D. E. Manolopoulos, Efficient stochastic thermostatting of path integral molecular dynamics, J. Chem. Phys. **133**, 124104 (2010).

[81] S. Azadi, R. Singh, and T. D. Kühne, Nuclear quantum effects induce metallization of dense solid molecular hydrogen, J. Comput. Chem. **39**, 262 (2018).

[82] N. Holmes (unpublished).

[83] W. M. Rankine, On the thermodynamic theory of waves of finite longitudinal disturbance, in *Classic Papers in Shock Compression Science* (Springer, Berlin, 1998), pp. 133–148.

[84] D. G. Hicks, T. R. Boehly, P. M. Celliers, J. H. Eggert, S. J. Moon, D. D. Meyerhofer, and G. W. Collins, Laser-driven single shock compression of fluid deuterium from 45 to 220 GPa, Phys. Rev. B **79**, 014112 (2009).

[85] M. D. Knudson and M. P. Desjarlais, High-Precision Shock Wave Measurements of Deuterium: Evaluation of Exchange-Correlation Functionals at the Molecular-To-Atomic Transition, Phys. Rev. Lett. **118**, 035501 (2017).

[86] G. V. Boriskov, A. I. Bykov, R. IlKaev, V. D. Selemir, G. V. Simakov, R. F. Trunin, V. D. Urlin, A. N. Shuikin, and W. J. Nellis, Shock compression of liquid deuterium up to 109 GPa, Phys. Rev. B **71**, 092104 (2005).

[87] R. D. Dick and G. I. Kerley, Shock compression data for liquids. II. condensed hydrogen and deuterium, J. Chem. Phys. **73**, 5264 (1980).

[88] W. J. Nellis, A. C. Mitchell, M. Van Thiel, G. J. Devine, R. J. Trainor, and N. Brown, Equation-of-state data for molecular hydrogen and deuterium at shock pressures in the range 2–76 GPa (20–760 kbar), J. Chem. Phys. **79**, 1480 (1983).

[89] M. Ruggeri, M. Holzmann, D. M. Ceperley, and C. Pierleoni, Quantum monte carlo determination of the principal Hugoniot of deuterium, Phys. Rev. B **102**, 144108 (2020).

[90] M. D. Knudson, D. L. Hanson, J. E. Bailey, C. A. Hall, J. r. Asay, and C. Deeney, Principal Hugoniot, reverberating wave, and mechanical reshock measurements of liquid deuterium to 400 GPa using plate impact techniques, Phys. Rev. B **69**, 144209 (2004).

[91] Z. He, Q. Zhang, H. Liu, G. Jia, X. Huang, Z. Fang, Z. Xie, J. Ye, H. Shu, J. Dong *et al.*, High-precision equation of state benchmark for cryogenic liquid deuterium at ultrahigh pressure, Phys. Rev. B **103**, 134107 (2021).

[92] N. C. Holmes, M. Ross, and W. J. Nellis, Temperature measurements and dissociation of shock-compressed liquid deuterium and hydrogen, Phys. Rev. B **52**, 15835 (1995).

[93] G. Collins, P. Celliers, L. Da Silva, R. Cauble, D. Gold, M. Foord, N. Holmes, B. Hammel, R. Wallace, and A. Ng, Temperature Measurements of Shock Compressed Liquid Deuterium up to 230 GPa, Phys. Rev. Lett. **87**, 165504 (2001).

[94] P. Loubeyre, S. Brygoo, J. Eggert, P. M. Celliers, D. K. Spaulding, J. R. Rygg, T. R. Boehly, G. W. Collins, and R. Jeanloz, Extended data set for the equation of state of warm dense hydrogen isotopes, Phys. Rev. B **86**, 144115 (2012).

[95] J. E. Bailey, M. D. Knudson, A. L. Carlson, G. S. Dunham, M. p. Desjarlais, D. L. Hanson, and J. R. Asay, Time-resolved optical spectroscopy measurements of shocked liquid deuterium, Phys. Rev. B **78**, 144107 (2008).

[96] W. Kołos and L. Wolniewicz, Accurate computation of vibronic energies and of some expectation values for H_2, D_2, and T_2, J. Chem. Phys. **41**, 3674 (1964).